

Novel Spin-Orbit Torques using Selenium-Based 2D Materials and Light-Element Aluminum

Richa Mudgal



Department of Physics
Indian Institute of Technology Delhi
January 2025

© **Indian Institute of Technology Delhi (IITD), New Delhi, 2025**

Novel Spin-Orbit Torques using Selenium-Based 2D Materials and Light-Element Aluminum

by

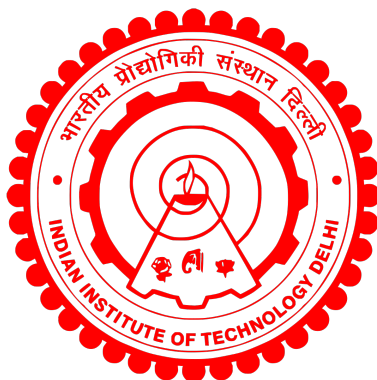
Richa Mudgal

Department of Physics

Submitted

in fulfilment of the requirements for the degree of Doctor of Philosophy

to the



Indian Institute of Technology Delhi

January 2025

Certificate

This is to certify that the thesis entitled, **Novel Spin-Orbit Torques using Selenium-Based 2D Materials and Light-Element Aluminum**, being submitted by **Ms. Richa Mudgal** to the Department of Physics, Indian Institute of Technology Delhi, for the award of the degree of **Doctor of Philosophy** is a record of bonafide work carried out by her. She has worked under our supervision and guidance and has fulfilled the requirements for the submission of this thesis, which in our opinion has reached the requisite standard.

The results contained in this thesis have not been submitted, in part or full, to any other University or Institute for the award of any degree/diploma.

Dr. Pranaba Kishor Muduli

Professor

Dept. of Physics

IIT Delhi, 110016

India

Date:

Dr. Samaresh Das

Professor

Dept. of Physics

IIT Delhi, 110016

India

Date:

Acknowledgement

Firstly, I would like to express my gratitude to my supervisors, Prof. P.K. Muduli and Prof. Samaresh Das, for proposing the thesis problem and supervising the work. I am indebted to them for their constant support and encouragement throughout the duration of my Ph.D. I consider myself fortunate to have had the opportunity to work closely with two experts in the field, who have significantly enhanced the quality of the present thesis with their specialized inputs and suggestions. Without their congenial demeanor and intellectual support, this thesis would not have been completed.

I would also like to extend my sincere thanks to the departmental members of my research committee, Prof. Rajendra Singh and Prof. Pintu Das, for their valuable feedback and suggestions during various presentations. I am grateful to the external SRC member, Dr. Ankur Goswami, for encouraging me to learn the fundamentals of Physics.

I would like to express my gratitude to Prof. Birabar Ranjit Kumar Nanda and Prof. Sashi Satpathy for allowing their student to perform the band structure calculation of PtSe₂ work. I am appreciative of their valuable input during various meetings to discuss the work. Additionally, I would like to thank Bubunu Biswal and Pratik Sahu for completing all the band structure calculations.

I thank Dr. Biswarup Satpati from Saha Institute of Nuclear Physics for his help in making cross-sectional TEM images of PtSe₂/NiFe heterostructure.

I am grateful to my senior labmate, Dr. Alka Jakhar, for teaching me the operation of various fabrication tools. I am thankful to her for her kind support during different research work in the early stage of my Ph.D and her readiness, even at odd times. I thank Pankhuri ma'am for teaching me the nuances of the STFMR set-up. I thank Dr. Sheetal Dewan for teaching me the operation of pulsed laser deposition technique. I appreciate Ram for providing support for DC planar Hall measurement.

I would like to thank Dr. Naveen Sisodia for providing us an insight into micromagnetic simulation using MuMax3 during the lockdown. I extend my gratitude to my other senior labmates, Dr. Niru Chowdhary, Dr. Aakash Kumar, Dr. Kacho Imtiyaaz Ali Khan, Dr. John Wilngton, Dr. Harman, Dr. Sumit, Dr. Himanshu, and Rekha for their help and support.

I also thank my other batchmates and juniors Neha, Nidhi, Aman, Vaishali, Prabal, Suprovat, Pinki, Biswajit, Ujjawal, Uzer, Jasmeen, Alen and Jyoti.

I extend my gratitude to my esteemed colleagues cum friends at IIT Delhi, namely Dr. Preetam Singh and Dr. Gulshan Kumar, for their unwavering support and guidance during the ups and downs of my Ph.D. journey. I would also like to express my appreciation to my friends Nutan,

Ekta, Manu, and Jyoti Ma'am whose companionship brought me joy at various moments.

I am obliged to Dr. Mahendra Singh Chauhan for his consistent support and encouragement for going ahead.

I am thankful to both my brothers, Ayush and Anant, as well as my cousins cum friends, Aaradhna and Vibhuti, for their endless conversations and invaluable time during my PhD, which always left me feeling energized and excited.

Lastly, I wish to express my deepest gratitude to my parents, whose unwavering support and encouragement allowed me to pursue my own path. This thesis can not be completed without their unconditional love and support.

This thesis is dedicated to my parents.



Richa Mudgal

Abstract

Spin-orbit torque (SOT) is a phenomenon that emerged as a promising substitute for spin transfer torque. The concept of SOT is extensively utilized in magnetic memories, neuromorphic computing, domain-wall motion, spintronics-based Radio frequency (RF) oscillators, etc. A SOT device consists of a heavy metal (HM)/ferromagnet (FM) heterostructure, where HM is used as the spin-current source. Spin Hall effect (SHE) and Rashba-Edelstein effect (REE) are the mechanisms that are commonly utilized to generate spin current in HM metal. However, the SOT-based devices are still far from commercialization due to the limited charge-to-spin efficiency of HM and restricted polarization of spin current, which always lies in the plane due to the symmetry of SHE and REE. The search for novel materials reaches 2D materials, specifically Transition metal dichalcogenides (TMDs), which are promising for SOT application due to their large spin-orbit coupling (SOC) coupling and ability to be deposited down to monolayers. The low crystal symmetries of TMDs are predicted to generate out-of-plane polarization, which is not possible by the spin Hall effect and Rashba-Edelstein effect. This eliminates the need for an external magnetic field to achieve SOT switching of perpendicular magnetization of FM materials. Apart from conventional effects (SHE and REE), which utilized bulk SOC of materials, there are some unconventional ways of generating spin current, which can be realized even in light elements having negligible SOC. These effects include the orbital Hall effect, orbital Rashba effect, spin swapping effect, etc. Due to the abundance of light elements, the utilization of these materials for SOT application can significantly reduce the cost of the device. In this thesis, we extensively studied spin-orbit torque in two types of materials: Selenium-based 2D materials (PtSe₂, PdSe₂, and GeSe) and light element Al. We employed spin-torque ferromagnetic resonance measurement (STFMR) to quantify charge-to-spin conversion efficiency and torque conductivities in these materials.

First, we measured spin-orbit torque utilizing STFMR in PtSe₂/NiFe heterostructure. We extensively studied frequency-dependent STFMR and angle-resolved STFMR for PtSe₂/NiFe/Pt system and separated out the effect of PtSe₂ in charge-to-spin conversion efficiency. The efficiency was found to be 0.1nm⁻¹ for PtSe₂, which results in an enhancement of 63% in effective SOT efficiency compared to that for the control sample (NiFe/Pt). This enhancement in efficiency value was further verified by DC planar Hall measurements. Our findings indicate that the interface between PtSe₂ and NiFe can generate a significant current-induced damping-like torque. Our band structure calculations suggest that the proximity magnetic field in the interfacial PtSe₂ plays an essential role in the strong charge-to-spin conversion observed in our samples. Our work demonstrates a novel form of SOT to obtain high charge-to-spin conversion

efficiencies for device applications. Additionally, our work demonstrates that "SOT through a proximity magnetic field" needs to be considered for explaining SOT observed in other TMD-based material systems.

We further studied the spin-orbit torque in PdSe₂/NiFe/AlO_x heterostructure, where AlO_x was used as the capping layer. We performed a complete angle-resolved STFMR to separate out the contribution of different spin polarizations in the spin-orbit torques. We observed a substantial damping-like torque corresponding to the y -polarization of spin current, which is found to be the opposite compared to the control sample (NiFe/AlO_x). In addition, we observed an unconventional field-like torque corresponding to the x -polarization of spin current, which is not allowed by conventional mechanisms such as SHE and REE. We anticipate that unconventional polarization is arising due to the low crystal symmetry of PdSe₂, while conventional torque arises likely due to the finite spin splitting caused by magnetic proximity.

Next, We studied spin-orbit torque in GeSe/NiFe/AlO_x heterostructure. First, we optimized the growth of GeSe using the pulsed laser deposition method. We measured angle resolved STFMR for GeSe-GeO_x/NiFe/AlO_x and compared the results with the control sample (NiFe/AlO_x). We observed a large damping-like torque in the GeSe-based stack, which was absent in the control sample. By using different control measurements, we exclude the contribution of bulk GeSe to the measured spin-orbit torque. We believe that the oxygen gradient due to the native oxidation of GeSe film at the GeSe and NiFe interface is responsible for generating a damping-like torque in the GeSe-based system via the orbital REE.

We also studied spin-orbit torque due to light element Al using Al/NiFe/AlO_x heterostructure. We found a large in-plane field-like torque corresponding to out-of-plane polarization of spin current, which was absent in the control sample (NiFe/AlO_x). We further observed that the magnitude of torque is independent of the Al thickness. In order to gain insight, we performed various controlled measurements by replacing Al with Pt to exclude the possibility of orbital torque. Our results are consistent with the theory of spin-swapping effects. We believe the observation of various novel SOTs reported in this thesis will be useful for various spintronics applications.

सारांश

स्पिन-ऑर्बिट टॉर्क (SOT) एक ऐसी घटना है जो स्पिन ट्रांसफर टॉर्क (STT) के लिए एक आशा जनक विकल्प के रूप में उभरी है। SOT की अवधारणा व्यापक रूप से मैग्नेटिक मेमोरी, न्यूरोमार्फिक गणना, डोमेन वाल की गति, स्पिनट्रॉनिक्स आधारित रेडियो आवृत्ति दोलक इत्यादि में उपयोग किया जाता है। एक SOT उपकरण में भारी धातु/चुम्बकीय पदार्थ का हेटेरोस्ट्रक्चर होता है, जहाँ भारी धातु स्पिन करेंट के स्रोत के रूप में उपयोग किया जाता है। स्पिन हॉल इफेक्ट (SHE) और रशबा-एडेलस्टीन इफेक्ट (REE) ऐसी क्रिया-विधि हैं जो साधारणतयः भारी धातु में स्पिन करेंट उत्पन्न करने के लिए उपयोग की जाती हैं। तथापि SOT उपकरण सीमित आवेश से स्पिन स्थानांतरण की दक्षता तथा प्रतिबंधित स्पिन ध्रुवीकरण के कारण अभी भी व्यावसायीकरण से दूर है। नए पदार्थ की खोज द्वि विमीय पदार्थ, विशेषतया ट्रांजीशन मेटल डाईचालकोजेनाइट्स (TMDs) तक पहुँचती है, जो अपने दीर्घ स्पिन ऑर्बिट कपलिंग (SOC) और एक परत तक निक्षेपित होने की क्षमता के कारण SOT अनुप्रयोगों के लिए आशाजनक हैं। TMDs की निम्न क्रिस्टल समरूपता से सतह के लंबवत पोलराइजेशन उत्पन्न होने की सम्भावना व्यक्त की गई है, जो SHE और REE से संभव नहीं है। यह चुंबकीय पदार्थ की लंबवत चुंबकत्व की SOT स्विचिंग प्राप्त करने के लिए बाह्य चुंबकीय क्षेत्र की आवश्यकता समाप्त कर देता है। पारम्परिक प्रभावों (SHE और REE), जिसमें पदार्थों का बल्क SOC का उपयोग किया जाता है, के अलावा स्पिन धारा उत्पन्न करने के कुछ अपरंपरागत तरीके हैं, जिन्हें यहां तक कि नगण्य SOC वाले हल्के तत्वों में भी देखा जा सकता है। इन प्रभावों में ऑर्बिटल हॉल इफेक्ट, ऑर्बिटल रशबा इफेक्ट, स्पिन स्वैपिंग इफेक्ट, आदि शामिल हैं। हलके तत्वों की प्रचुरता के कारण SOT अनुप्रयोग के लिए इन पदार्थों का उपयोग उपकरण की लागत को काफी कम कर सकता है। इस शोध प्रबंध में, हमने दो प्रकार के पदार्थों सेलेनियम आधारित 2D पदार्थ (PtSe₂, PdSe₂, और GeSe) और हलके तत्व एलुमिनियम में SOT का बड़े पैमाने पर अध्ययन किया। हमने इन पदार्थों में टॉर्क कंडक्टिविटी और आवेश से स्पिन रूपांतरण दक्षता मापने के लिए Spin Torque Ferromagnetic Resonance (STFMR) मापन विधि का प्रयोग किया।

सबसे पहले, हमने PtSe₂/NiFe हेटरो संरचना में STFMR का उपयोग करके SOT को मापा। हमने व्यापक रूप से PtSe₂/NiFe/Pt सिस्टम के लिए frequency dependent और angle resolved STFMR का अध्ययन किया और आवेश से spin रूपांतरण दक्षता में PtSe₂ के प्रभाव को अलग किया। PtSe₂ के लिए दक्षता -0.१ nm⁻¹ पाई गयी, जिसके परिणामस्वरूप control sample (NiFe/Pt) की तुलना में SOT की प्रभावी दक्षता में 63% की वृद्धि हुई। दक्षता मूल्य में इस वृद्धि को आगे direct current surface hall measurement द्वारा और सत्यापित किया गया। हमारे निष्कर्ष संकेत देते हैं कि PtSe₂ और NiFe के बीच का interface एक महत्वपूर्ण current induced damping like torque उत्पन्न कर सकता है। हमारी band structure गणना से पता चलता है कि interfacial PtSe₂ में proximity magnetic field मजबूत आवेश से स्पिन रूपांतरण में एक आवश्यक भूमिका निभाता है। हमारा काम उपकरण अनुप्रयोगों के लिए उच्च आवेश से स्पिन रूपांतरण प्राप्त करने के लिए SOT का एक नया रूप प्रदर्शित करता है। इसके अतिरिक्त, हमारा काम दर्शाता है कि अन्य TMDs आधारित systems में देखे गए SOT को समझने के लिए "Proximity Magnetic Field के द्वारा उत्पन्न SOT" पर विचार करने की आवश्यकता है।

हमने आगे PdSe₂/NiFe/AIO_x हेटेरो संरचना में SOT का अध्ययन किया, जहां AIO_x का उपयोग capping layer के रूप में किया गया था। SOT में विभिन्न spin polarizations के योगदान को अलग करने के लिए हमने एक पूर्ण angle resolved STFMR मापन किया। हमने स्पिन धारा के y-polarization के अनुरूप संतोषजनक damping like torque देखा, जो control sample (NiFe/AIO_x) की तुलना में विपरीत पाया गया। इसके अलावा, हमने स्पिन धारा के x-polarization के अनुरूप एक अपरंपरागत field like torque देखा, जिसकी व्याख्या SHE Spin और REE जैसे पारंपरिक प्रभावों द्वारा नहीं की जा सकती। हमारा अनुमान है कि अपरंपरागत polarization PdSe₂ की कम क्रिस्टल समरूपता के कारण उत्पन्न हो रहा है। जबकि पारंपरिक आघूर्ण, magnetic proximity के कारण होने वाले परिमित spin-splitting से उत्पन्न होने की संभावना है।

इसके बाद, हमने GeSe/NiFe/AIO_x हेटेरो संरचना में SOT का अध्ययन किया। सबसे पहले, हमने pulsed laser deposition विधि का उपयोग करके GeSe की growth को optimize किया। हमने GeSe-GeO_x/NiFe/AIO_x के लिए angle resolved STFMR का मापन किया और control sample (NiFe/AIO_x) के साथ परिणामों की तुलना की। हमने GeSe-आधारित structure में एक damping like torque देखा जो control sample में अनुपस्थित था। विभिन्न नियंत्रित मापों का उपयोग करके हमने पाया कि SOT में bulk GeSe का योगदान नगण्य था। हमारा मानना है कि GeSe और NiFe के interface पर GeSe परत के स्वाभाविक ऑक्सीकरण के कारण ऑक्सीजन प्रवणता GeSe आधारित system में orbital REE के द्वारा damping like torque उत्पन्न करने के लिए उत्तरदायी है।

हमने Al/NiFe/AIO_x हेटेरो संरचना का उपयोग करके हल्के तत्व Al के कारण SOT का भी अध्ययन किया। हमें out of plane polarization के संगत in-plane field like torque प्राप्त हुआ। हमने आगे देखा कि आघूर्ण का परिमाण Al की मोटाई से स्वतंत्र है। अंतर्दृष्टि प्राप्त करने के लिए, हमने orbital torque की सम्भावना को निष्काषित करने के लिए Al को Pt से प्रतिस्थापित करके विभिन्न control measurements किये। हमारे परिणाम spin swapping effect के सिद्धांत के अनुरूप हैं। हम मानते हैं कि इस शोध-प्रबंध में बताये गए विभिन्न नए SOTs विभिन्न स्पिनट्रॉनिक्स अनुप्रयोगों के लिए उपयोगी होंगे।

Contents

Certificate	i
Acknowledgements	ii
Abstract	iv
List of figures	xxv
List of tables	xxvi
1 Basics of Spintronics	1
1.1 Introduction: Spintronics	1
1.2 Spin current	3
1.3 Magnetization dynamics and ferromagnetic resonance	4
1.3.1 Spin Pumping	6
1.4 Spin-orbit interaction and spin-orbit torque	8
1.5 Generation of Spin Current using spin-orbit interaction	9
1.5.1 Spin Hall Effect	9
1.5.2 Rashba-Edelstein effect	12
1.5.3 Orbital Hall Effect	13
1.5.4 Orbital Rashba-Edelstein effect	14
1.5.5 Spin swapping effect	15

1.5.6	Unconventional Spin Polarization	16
1.6	Detection of Spin current	17
1.6.1	Spin torque ferromagnetic resonance	17
1.7	Motivation of Thesis	20
1.7.1	Thesis outline	22
2	Experimental Techniques	23
2.1	Thin film deposition	23
2.1.1	Magnetron Sputtering:	23
2.1.2	Pulsed Laser Deposition	25
2.1.3	Chemical Vapor Deposition:	27
2.2	Fabrication of Devices	28
2.2.1	Exposure and pattern development	28
2.2.2	Ion-milling	31
2.3	Structural Characterization	32
2.3.1	X-Ray Diffraction	32
2.3.2	Raman Spectroscopy	35
2.3.3	X-Ray Photoelectron Spectroscopy	37
2.3.4	Atomic Force Microscopy	39
2.4	Static Magnetic Measurement	41
2.4.1	SQUID Measurement	41
2.5	Dynamic Magnetic Measurement	42
2.5.1	Ferromagnetic resonance	42
2.5.2	Spin Torque Ferromagnetic Resonance	44

3	Magnetic Proximity induced efficient charge-to-spin conversion in large area PtSe₂/Ni₈₀Fe₂₀ heterostructures	50
3.1	Introduction	50
3.2	Experimental details and structural characterization	52
3.2.1	Optimization of growth of PtSe ₂	52
3.2.2	Structural characterization	52
3.2.3	Thickness dependent Raman spectra	54
3.2.4	Device fabrication	55
3.3	Results and discussion	55
3.3.1	Spin torque ferromagnetic resonance of PtSe ₂ /NiFe	55
3.3.2	Angular resolved spin-torque ferromagnetic resonance	58
3.3.3	Quantification of spin-orbit torque	60
3.3.4	Interfacial charge to spin conversion coefficient from V _S /V _A method	61
3.3.5	Determination of field-like torque	64
3.3.6	Determination of SOT using dc planar Hall effect measurement	66
3.3.7	Band structure calculation for PtSe ₂ /NiFe	68
3.4	Summary	70
4	Spin-orbit torque in PdSe₂/NiFe/AlO_x	71
4.1	Introduction	71
4.2	Results and Discussion	72
4.2.1	Structural characterization of PdSe ₂ thin films	72
4.2.2	Anisotropic magnetoresistance	73
4.2.3	STFMR measurements	74

4.2.4	Angular dependence of STFM	75
4.2.5	Discussion on the origin of spin-torque in PdSe ₂ /NiFe	77
4.3	Summary	78
5	Large Damping-like torque in GeSe-GeO_x/NiFe/AlO_x	79
5.1	Introduction	79
5.2	Results and Discussion	81
5.2.1	Growth optimization and structural characterization	81
5.2.2	XPS depth profiling	84
5.2.3	Study of Spin Pumping	84
5.2.4	Spin-Torque Ferromagnetic Resonance	86
5.3	Summary	89
6	Observation of a Nontrivial In-Plane Field-Like Torque due to Out-of-Plane Spin Polarization in Al/Ni₈₀Fe₂₀/AlO_x Heterostructures	91
6.1	Introduction	91
6.2	Experimental details	92
6.3	Results and discussion	93
6.3.1	Nontrivial spin torque in Al/Ni ₈₀ Fe ₂₀ /AlO _x	93
6.3.2	Role of orbital Hall effect	96
6.3.3	Origin of non-trivial spin torque in Al/Ni ₈₀ Fe ₂₀ /AlO _x	99
6.3.4	Impact of NiFe thickness on the torque conductivity	99
6.3.5	Origin of non-trivial torque in Pt/NiFe/AlO _x	100
6.3.6	Role of ferromagnetic layer	102
6.4	Summary	102

7 Summary and Future outlook	104
7.1 Summary of the thesis	104
7.2 Major Outcomes	105
7.2.1 Chapter 3: Magnetic Proximity induced efficient charge-to-spin conversion in large area PtSe ₂ /Ni ₈₀ Fe ₂₀ heterostructures	105
7.2.2 Chapter 4: Spin-orbit torque in PdSe ₂ /NiFe/AlO _x heterostructure	105
7.2.3 Chapter 5: Large Damping-like torque in GeSe-GeO _x /NiFe/AlO _x	106
7.2.4 Chapter 6: Observation of a Nontrivial In-Plane Field-Like Torque due to Out-of-Plane Spin Polarization in Al/Ni ₈₀ Fe ₂₀ /AlO _x Heterostructures	107
7.3 Future Outlook	107
References	109
Appendix	120
A Details of computational methods and additional results	120
A.1 Density-functional Methods	120
A.2 Design of the Permalloy and the PtSe ₂ /NiFe interface structures for density-functional calculations	120
A.3 Calculation of the Rashba Coefficient	122
A.4 Proximity magnetic field	122
Publication	124
Biodata	128

List of Figures

1.1	(a) Magnetoresistance of three Fe/Cr superlattices at 4.2 K. The current and the applied field are along the same [110] axis in the plane of the layers [6].(b) Schematic of spin-dependent scattering in magnetic multilayers	2
1.2	Schematic representation of the flow of (a) unpolarized current (b) spin-polarized current (c) pure spin current. Red and blue arrows depict spin up and spin down, respectively, while the green arrow is the direction of flow	4
1.3	(a) Schematic of magnetization precession in the presence of external field; (b) Damped precession of magnetization about the external field	5
1.4	Schematic of magnetization precession under resonance condition	5
1.5	Schematic of spin pumping from ferromagnetic layer to non-magnetic layer	7
1.6	Schematic of spin Hall effect	10
1.7	Schematic representation of spin current generated by (a)intrinsic mechanism, (b) skew scattering, and (c) side jump	11
1.8	(a) Schematic of Rashba-Edelstein effect in a heterostructure of FM/NM (b) Shift of fermi contour in the presence of charge current	12
1.9	Schematic representation of orbital Hall effect	13
1.10	(a) Schematic representation of orbital Rashba-Edelstein effect (b) shift of Fermi contour in presence of charge current	14
1.11	Schematic representation of spin swapping effect	15
1.12	Schematic representation of various spin polarization	16

1.13	(a) Schematic of ferromagnetic resonance SOT device comprises of NM/FM heterostructure. (b) Schematic of resistance and current variation with time resulting in the oscillatory voltage having finite DC component. Figure adapted from Ref [54]	18
2.1	(a) Schematic representation of sputtering system (b) Target assembly in balanced magnetron configuration. N and S are the north and south poles of the magnet. The direction of magnetic field lines is shown with an arrow.	24
2.2	Schematic representation of pulsed laser deposition system	26
2.3	Schematic representation of low-pressure chemical vapor deposition system. T_1 and T_2 indicate two different temperatures. The vertical dotted line shows the two separate zones.	27
2.4	Schematic representation of various steps involved in device fabrication utilizing (a) Lift-off, (b) etching method	28
2.5	(a) Schematic representation of fabrication steps for microstrip pattern and coplanar waveguide (b) Image of laser writer set-up	30
2.6	Schematic representation of Ion milling using Ar ions	31
2.7	(a) Schematic of the diffracted x-rays showing the path difference between x-rays scattered from two consecutive atomic planes; (b) schematic of X-ray diffractometer consisting of X-ray source and detector. The direction of the incident and diffracted X-rays are shown in the figure.	32
2.8	X-ray diffractometer assembled for GI-XRD. The incident angle is kept fixed while the detector is rotated to find the Bragg's condition	33
2.9	(a) Schematic of x-rays reflected from the interface between the thin film and the substrate (b) X-ray reflectivity pattern consisting of information about thickness, density difference, and roughness	34
2.10	(a) Schematic of elastic and inelastic scattering of a photon from a tri-atomic molecule (b) Transition between energy level for Rayleigh stokes and antistokes line and corresponding spectra	35

2.11 Schematic of Raman spectroscopy setup	36
2.12 Schematic of X-ray scattering from an atom resulting ejection of photoelectron (b) Schematic of photoelectrons detector	38
2.13 Schematic of atomic force microscopy set-up	40
2.14 Schematic of SQUID magnetometer	41
2.15 (a) Schematic of ferromagnetic resonance set up (b) Zoom view of a co-planar waveguide with a sample (c) Schematic of coplanar waveguide indicating the direction of RF field	43
2.16 (a) Ferromagnetic resonance spectra of NiFe (10 nm)/AlO _x measured at different frequencies of RF field, (b) linewidth vs. frequency plot, and (c) frequency vs. resonance field. Symbols are measured data while the solid lines are fits.	44
2.17 Schematic of spin-torque ferromagnetic resonance set up.	45
2.18 (a) Variation of resistance with in-plane angle; (b) STFM _R spectra measured at 5 GHz frequency and at a fixed in-plane angle, $\theta=40^\circ$; (c) variation of linewidth with frequency; (d) variation of frequency with resonance field. In all the plots, the symbols are measured data while the solid lines are fits.	46
2.19 (a), (b) Symmetric and antisymmetric component of NiFe(10 nm)/Pt(2.5 nm) respectively measured at 6 GHz frequency. Symbols are measured data and solid lines are fit.	47
3.1 (a) Side view and (b) top view of PtSe ₂ . The dashed lines represent two mirror planes parallel to the lattice vectors a and b . solid black lines represent the unit cell of PtSe ₂	51

- 3.2 (a) Cross-sectional HRTEM image of PtSe₂/NiFe/Pt stack. The interface is indicated by the red dashed lines. The magnified view of the square region is shown in the bottom part of the figure, showing the formation of high-quality PtSe₂ lattices (with 1T structure). (b) Raman spectra of PtSe₂ thin film (red curve) and that of the device after deposition of NiFe/Pt (black curve). The spectra show two strong peaks labeled as E_g and A_{1g} and one shoulder peak labeled as longitudinal optical (LO) mode. (c) X-ray photoelectron spectra of Pt-4f core level. Spectra were fitted with four peaks corresponding to PtSe₂ and PtSe_x. Splitting between doublets of Pt-4f peaks is found to be 3.3 eV. 53
- 3.3 (a) X-ray diffraction pattern for PtSe₂ thin film exhibiting a single peak corresponding to (001)-plane. (b) Atomic force microscopy image showing step profile of PtSe₂ (for determining thickness). The *inset* shows a line profile along the step (blue line) (c) Measured in-plane hysteresis loop (VSM) for NiFe/Pt and PtSe₂/NiFe/Pt. 54
- 3.4 (a) Measured Raman spectra of PtSe₂/Py devices for different thicknesses of PtSe₂. For each thickness of PtSe₂, the data from two devices is shown and labeled as D1 and D2. The Raman intensity is normalized w.r.t the intensity of E_g mode. (b) The behavior of the intensity of A_{1g} mode normalized w.r.t the intensity of E_g mode with the thickness of PtSe₂. The intensity ratio is averaged over two devices. 54
-

- 3.5 (a) Schematic of sample stack showing the direction of RF current and the precession of magnetization. (b) Schematic of STFMR set-up consisting of an optical image of the device. Here, S represents the RF signal source. The directions of the RF current and applied field are also shown in the enlarged image. (c) Anisotropic magnetoresistance of PtSe₂ (10 nm)/NiFe (5 nm)/Pt (3 nm) together with control sample NiFe (5 nm)/Pt (3 nm). Frequency dependent STFMR spectra for (d) NiFe/Pt and (e) PtSe₂(10 nm)/NiFe/Pt measured at 50°. The spectra are shifted for clarity.(f) Example of STFMR spectra measured at 5 GHz and $\theta = 50^\circ$ for PtSe₂(t)/NiFe/Pt for varying thickness of PtSe₂ layer. The plots are shifted for clarity. 56
- 3.6 (a) The linewidth versus frequency for NiFe/Pt and PtSe₂(10 nm)/NiFe/Pt. The inset shows a variation of the Gilbert damping parameter (α) with the thickness of PtSe₂ (t_{PtSe_2}) in the PtSe₂/NiFe/Pt stack. The dashed line in the inset shows the average value of α for $t_{\text{PtSe}_2} \geq 6.5$ nm (b) variation of the Gilbert damping parameter (α) with the thickness of PtSe₂ (t_{PtSe_2}) in the PtSe₂/NiFe/Pt stack. The dashed line in the inset shows the average value of α for $t_{\text{PtSe}_2} \geq 6.5$ nm (c) Resonance field versus frequency for NiFe/Pt and PtSe₂(10 nm)/NiFe/Pt (d) Variation of effective magnetization with the thickness of PtSe₂ 57
- 3.7 Angular dependence of V_S and V_A for (a) NiFe/Pt (b) PtSe₂ (10 nm)/NiFe/Pt, measured at 5 GHz. In all the plots, symbols represent the measured data, while solid lines represent fits as described in the main text 58
- 3.8 Angular dependence of (a) symmetric and (b) antisymmetric component of V_{mix} measured at 5 GHz frequency. The solid green line shows the fit with Eq. (3.3 and 3.4) while the red line shows the fit without the $\sin 2\theta$ -term. (c) The angular dependence of V_S to show the effect of inclusion of $\sin \theta$ -term. The solid green line shows the fit with Eq. (3.5) while the red line shows the fit without the $\sin \theta$ -term. In all the plots, the symbols represent measured data. 59

3.9	(a) Variation of effective SOT efficiency with frequency for PtSe ₂ (10 nm)/NiFe/Pt and NiFe/Pt. Each data point for PtSe ₂ (10 nm)/NiFe/Pt is the average of three devices, with error bars denoting device-to-device variation. The dashed lines represent the average values. (b) Variation of effective SOT efficiency, $\xi_{\text{SOT}}^{\text{eff}}$ with t_{PtSe_2} . Each data point represents the average of three devices.	60
3.10	Comparison of q_{ICS} of different materials	64
3.11	(a) Measured S_{11} versus frequency for PtSe ₂ /NiFe/Pt and NiFe/Pt. (b) Corresponding RF current passing through the device for PtSe ₂ /NiFe/Pt and NiFe/Pt. (c) Frequency dependence of H_{total} and H_{Oe} for PtSe ₂ /NiFe/Pt and NiFe/Pt. (d) Odd component of resonance field versus dc current.	65
3.12	(a) Optical image of Hall cross-bar having dimension of $20\mu\text{m} \times 100\mu\text{m}$ and $10\mu\text{m} \times 80\mu\text{m}$ of the longitudinal and transverse channel respectively. The direction of current and the field are indicated in the image. Planar Hall resistance of (b) NiFe/Pt and (c) PtSe ₂ /NiFe/Pt for both polarity of DC current measured at constant external field of 1000 Oe (d) Difference between planar Hall resistance for positive and negative DC current. Out-of-plane field (H_{OOP}) vs. current density plot for (e) NiFe/Pt and (f) PtSe ₂ /NiFe/Pt symbols are measured data while solid lines correspond to the fitting.	66

- 3.13 Density functional theory results for the PtSe₂/NiFe interface. (a) Band structure of bulk PtSe₂ indicating the electron pocket at K and the hole pocket at Γ at the Fermi energy $E_F = 0$, and the type-II Dirac cone at D, along the $\Gamma - A$ line. *Inset* shows the Brillouin zone, where the electron (green circle) and hole pockets (red circles and crosses) have been indicated. (b) Band structure of (PtSe₂)₆/NiFe showing the bulk-like bands of PtSe₂ (red for Pt and green for Se) with electron and hole pockets at Γ and K, interspersed with the NiFe bands (thin lines). The BZ in PtSe₂/NiFe is different from that of PtSe₂, but the Γ is the same, and the projection of the K point has been indicated by the square bracket. (c) Electron charge density difference contours indicating charge transfer from NiFe to the PtSe₂ interface layer, due to the interface formation. The orange and purple colors indicate, respectively, the charge accumulation and depletion regions. 68
- 4.1 (a) Raman spectra of PdSe₂ thin film measured at different points, (b) Surface topography of PdSe₂ thin film measured using atomic force microscopy (c) Raman spectra of PdSe₂ film before and after deposition of NiFe 72
- 4.2 Variation of resistance with angle for (a) NiFe/AlO_x and PdSe₂/NiFe/AlO_x. Symbols are measured data and solid lines are fit. 73
- 4.3 STFM spectra of (a) NiFe (5 nm)/AlO_x (b) PdSe₂/NiFe (5 nm)/AlO_x devices measured at 5 GHz frequency and $\theta = 40^\circ$. The solid lines (black) represent a sum of symmetric (green) and antisymmetric (blue) Lorentzian functions, whereas the symbols represent measured data. 74
- 4.4 (a) Linewidth vs. frequency data, and (d) Frequency vs. resonance field data for PdSe₂/NiFe (5 nm)/AlO_x. Symbols are measured data, and solid lines are fits 75
- 4.5 Variation of (a) V_S and (b) V_A of NiFe (5 nm)/AlO_x and Variation of (c) V_S and (d) V_A of PdSe₂/NiFe (5 nm)/AlO_x device as a function of in-plane magnetic-field angle. The RF frequency and power are kept fixed at 5 GHz and +10 dBm, respectively. Symbols are measured data, and solid lines are fit using Eq. (4.1) and Eq. (4.2). 76
-

4.6	Calculated torque conductivities ($\sigma_{(DL,FL)}^{(x,y,z)}$) corresponding to different spin polarization for NiFe (5 nm)/AlO _x and PdSe ₂ /NiFe (5 nm)/AlO _x	77
5.1	(a) Variation of roughness and thickness with the working pressure. The value of roughness has been multiplied by 5 for clarity (b) XRD pattern of GeSe thin films deposited at different substrate temperature.	81
5.2	(a) X-ray reflectivity pattern of GeSe film measured using Cu $k\alpha$ X-rays (b) XRD pattern of GeSe thin films annealed at different temperatures. (c) Raman spectra of GeSe film annealed at different temperatures measured with a laser beam of 532 nm wavelength. Four characteristic peaks of GeSe are labeled as A _g ³ , B _{3g} ¹ , A _{3g} ¹ , and A _g ¹	82
5.3	Elemental mapping of GeSe thin films annealed at (a) 350°C, (b) 400°C, and (c) 450°C. The Bar in the vicinity of images shows the atomic percentage of Ge and Se atoms in the films; Atomic force micrograph of GeSe films annealed at (d) 350°C, (e) 400°C, and (f) 450°C.	83
5.4	(a) GeSe/NiFe stack indicating four different positions, where XPS has been recorded; X ray photoelectron spectra of (b) Ni 2p _{3/2} and (b) Ge 3d core level at four position. Spectra was measured at different depth by sputtering the stack as depicted in the figure (d) The variation of oxygen concentration from surface of GeSe thin film to the depth in vertical direction.	84
5.5	(a) Ferromagnetic resonance spectra of GeSe(2 nm)/NiFe (10 nm)/AlO _x measured at different frequencies of RF field varying from 3 GHz to 8.5 GHz; (b) frequency vs. resonance field plot for GeSe (t_{GeSe})/NiFe/AlO _x ; symbols are measured data, while solid lines are fitted plot in Kittel equation (c) Variation of linewidth with frequency for different thicknesses of GeSe varied from 0 nm to 12 nm (d) Variation of damping parameter with GeSe thickness. Dotted lines are the average of the damping constant	85

5.6	(a) STFM spectra of GeSe/NiFe/Al measured at 6 GHz frequency with an angle of 220° between RF current and external field. Data was fitted in the equation 2.6, and symmetric and anti-symmetric parts are shown separately also. (b) The variation of resistance with the in-plane angle for NiFe/ AlO_x and GeSe/NiFe/ AlO_x . Symbols are measured resistance and the solid line is fit as discussed in the text; Variation of V_S and V_A with the in-plane angle for NiFe/ AlO_x ((c), (d)) and GeSe/NiFe/ AlO_x ((e), (f)) In all the plots, symbols are measured data and solid lines are fit.	87
5.7	The calculated torque conductivities σ_{FL}^y , σ_{DL}^y and σ_{FL}^z for NiFe/ AlO_x and GeSe (12 nm)/NiFe/ AlO_x	88
5.8	Schematic presentation of the possible origin of torque arising in GeSe- GeO_x /NiFe heterostructure as discussed in the text.	89
6.1	(a) The magnetization data for Al (2 nm)/Py/ AlO_x ; X-ray photoelectron spectra of (b) Ni 2p core level, and (c) Al 2p core level	93
6.2	(a) Schematic of the ST-FMR measurement setup together with the structure of the ST-FMR device (Al/Py). The RF current is applied along the x -direction, while the magnetization direction, θ is varied in the xy -plane. (b) Example of STFM spectra of Al (2 nm)/Py (10 nm)/ AlO_x devices measured at 6 GHz frequency and $\theta = 40^\circ$. The solid lines (black) represent a sum of symmetric (green) and antisymmetric (blue) Lorentzian functions, whereas the symbols represent measured data. (c) Linewidth vs. frequency data, and (d) Frequency vs. resonance field data for Al (2 nm)/Py/ AlO_x . Symbols are measured data, and solid lines are fits. Inset shows the magnetization data for Al (2 nm)/Py/ AlO_x	94

- 6.3 Variation of (a) V_S and (b) V_A of Al (2 nm)/Py (10 nm)/AlO_x device as a function of in-plane magnetic-field angle. The RF frequency and power are kept fixed at 6 GHz and +6 dBm, respectively. Symbols are measured data, and solid lines are fit using Eq. (6.1) and Eq. (6.2). (c) Calculated torque conductivities σ_{FL}^z , σ_{DL}^y and σ_{DL}^z with Al thickness, d . The torque conductivity, σ_{DL}^z is multiplied by a factor of 3 to enhance the visibility in the plot. The dashed line represents the average value of σ_{FL}^z 95
- 6.4 (a) M-H plot for Pt(2.5)/Py(10)/AlO_x, and (b) frequency vs. resonance field plot for Pt(2.5)/Py(10)/AlO_x. Symbols represent measured data, while the solid line represents the fit with the Kittel equation. 97
- 6.5 (a) Example of STFMR spectra of Pt(2.5 nm)/Py(10 nm)/AlO_x devices measured at 6 GHz frequency and $\theta = 40^\circ$. The solid lines (black) represent a sum of symmetric (green) and antisymmetric (blue) Lorentzian functions, whereas the symbols represent measured data. Variation of (b) V_S and (c) V_A of Pt(2.5 nm)/Py(10 nm)/AlO_x device as a function of in-plane magnetic-field angle. The RF frequency is kept fixed at 6 GHz. Symbols are measured data, and solid lines are fit using Eq. (6.1) and Eq. (6.2). (d) Calculated torque conductivities σ_{FL}^z , σ_{DL}^y and σ_{DL}^z for Pt(2.5 nm)/Py(10 nm)/AlO_x device. The torque conductivity, σ_{DL}^z is multiplied by a factor of 3 to enhance the visibility in the plot. 98
- 6.6 (a) V_S and (b) V_A of Al(7 nm)/Py(5 nm)/AlO_x device as a function of in-plane magnetic field angle. The RF frequency is kept fixed at 6 GHz. Symbols are measured data, and solid lines are fit using Eq. 6.1 and 6.2. (c) Calculated torque conductivities σ_{FL}^z , and σ_{DL}^y for Al(7 nm)/Py(5 nm)/AlO_x device. 100
- 6.7 Variation of (a) V_S , and (b) V_A for Pt(5)/Py(10)/AlO_x as a function of in-plane magnetic field angle. The RF frequency is kept fixed at 6 GHz. Symbols are measured data, and solid lines are fit using Eq. 6.1 and 6.2; (c) Calculated torque conductivities σ_{FL}^z , and σ_{DL}^y for Pt(5 nm)/Py(10 nm)/AlO_x device. 100
-

6.8	Variation of (a) V_S , and (b) V_A for Pt(5)/Py(10)/AlO _x as a function of in-plane magnetic field angle. The RF frequency is kept fixed at 6 GHz. Symbols are measured data, and solid lines are fit using Eq. 6.1 and 6.2; (c) Calculated torque conductivities σ_{FL}^z , and σ_{DL}^y for Pt(5 nm)/Py(10 nm)/AlO _x device. . . .	101
6.9	(a) Ferromagnetic resonance spectra for CoFeB(10 nm)/AlO _x ; Variation of (b) linewidth with frequency (c) frequency with resonance field. In all the plots, symbols are measured data, and solid lines are fits as mentioned in the text . . .	102
6.10	(a) Anisotropic magnetoresistance for CoFeB (10 nm)/AlO _x , (b), (c) STFM spectra for CoFeB (10 nm)/AlO _x (d) Anisotropic magnetoresistance for Al(2 nm)/CoFeB (10 nm)/AlO _x , (e), (f) STFM spectra for Al(2 nm)/CoFeB (10 nm)/AlO _x . STFM was measured at 4 GHz frequency for $\theta = 45^\circ$ and 135° . . .	103
A1	The crystal structure of (PtSe ₂) ₄ /NiFe hetero-interface.	121
A2	(a) The atomic projected band structure of (PtSe ₂) ₄ /Ni. The red and green colors represent the Pt and Se contributions, respectively. The inset shows the clear Rashba spin splitting of the electrons in the Γ electron pocket. (b, c) The spin texture of the Rashba-split bands, a and b, with the arrows representing the x and y components of the spin, and the color representing the z component. . .	121
A3	The non-magnetic (left panel) and magnetic (middle panel) band structures of (PtSe ₂) ₁ /Ni. Right panel shows the magnetic band structure of (PtSe ₂) ₁ /NiFe. The green and red colors represent the spin-up and spin-down bands, respectively, which are split due to the proximity magnetic field. Here, SOC is not included in all calculations, so that green (red) bands are pure spin up (down) states. The size of the circles indicates the contributions from the PtSe ₂ orbitals so that the PtSe ₂ bands appear as more prominent, thicker lines. The energy splitting between the PtSe ₂ -dominated spin-up and spin-down bands at certain k-points are indicated by arrows, from which the estimated value of the spin-splitting is determined to be $\Delta E \sim 0.10 - 0.15$ eV. Here, and throughout the paper, the Fermi energy $E_F = 0$	123

List of Tables

2.1 Torque generated by different polarization and their contribution in voltage component	48
4.1 The magnitude of different components of V_S and V_A for PdSe ₂ /NiFe/AlO _x and NiFe/AlO _x	76